Exp Fluids (2017) 58:75
DOI 10.1007/s00348-017-2347-5

RESEARCH ARTICLE

A rotating annulus driven by localized convective forcing: a new atmosphere-like experiment

Hélène Scolan[1] · **Peter L. Read**[1]

Received: 21 November 2016 / Revised: 7 April 2017 / Accepted: 10 April 2017

Abstract We present an experimental study of flows in a cylindrical rotating annulus convectively forced by local heating in an annular ring at the bottom near the external wall and via a cooled circular disk near the axis at the top surface of the annulus. This new configuration is distinct from the classical thermally driven annulus analogue of the atmosphere circulation, in which thermal forcing is applied uniformly on the sidewalls, but with a similar aim to investigate the baroclinic instability of a rotating, stratified flow subjected to zonally symmetric forcing. Two vertically and horizontally displaced heat sources/sinks are arranged, so that in the absence of background rotation, statically unstable Rayleigh–Bénard convection would be induced above the source and beneath the sink, thereby relaxing strong constraints placed on background temperature gradients in previous experimental configurations based on the conventional rotating annulus. This better emulates local vigorous convection in the tropics and polar regions of the atmosphere while also allowing stably-stratified baroclinic motion in the central zone of the annulus, as in mid-latitude regions in the Earth's atmosphere. Regimes of flow are identified, depending mainly upon control parameters that in turn depend on rotation rate and the strength of differential heating. Several regimes exhibit baroclinically unstable flows which are qualitatively similar to those previously observed in the classical thermally driven annulus. However, in contrast to the classical configuration, they typically exhibit more spatio-temporal complexity. Thus, several regimes of flow demonstrate the equilibrated coexistence of, and interaction between, free convection and baroclinic wave modes. These new features were not previously observed in the classical annulus and validate the new setup as a tool for exploring fundamental atmosphere-like dynamics in a more realistic framework. Thermal structure in the fluid is investigated and found to be qualitatively consistent with previous numerical results, with nearly isothermal conditions, respectively, above and below the heat source and sink, and stably-stratified, sloping isotherms in the near-adiabatic interior.

1 Introduction

The circulation of the atmosphere is the result of several physical forcing processes: gravity, rotation, radiative exchanges (incoming sunlight, outgoing thermal infrared radiation), clouds and moisture processes, chemical reactions, interaction with surface topography, boundary processes, etc. Although numerical global circulation models solving equations of dynamics, thermodynamics, and continuity in 3D on a sphere are capable of reproducing and even predicting many features of the observed atmosphere, their complexity and the need to represent unresolved processes by semi-empirical parameterizations mean that insights and understanding of how the real atmosphere works may still be elusive.

In this context, laboratory analogues of the dynamics of the atmosphere continue to help scientists understand fundamental dynamical processes in the atmosphere by

Electronic supplementary material The online version of this article (doi:10.1007/s00348-017-2347-5) contains supplementary material, which is available to authorized users.

✉ Hélène Scolan
helene.scolan@physics.ox.ac.uk

Peter L. Read
peter.read@physics.ox.ac.uk

[1] Department of Physics, Atmospheric, Oceanic and Planetary Physics, University of Oxford, Oxford, UK

Published online: 23 May 2017

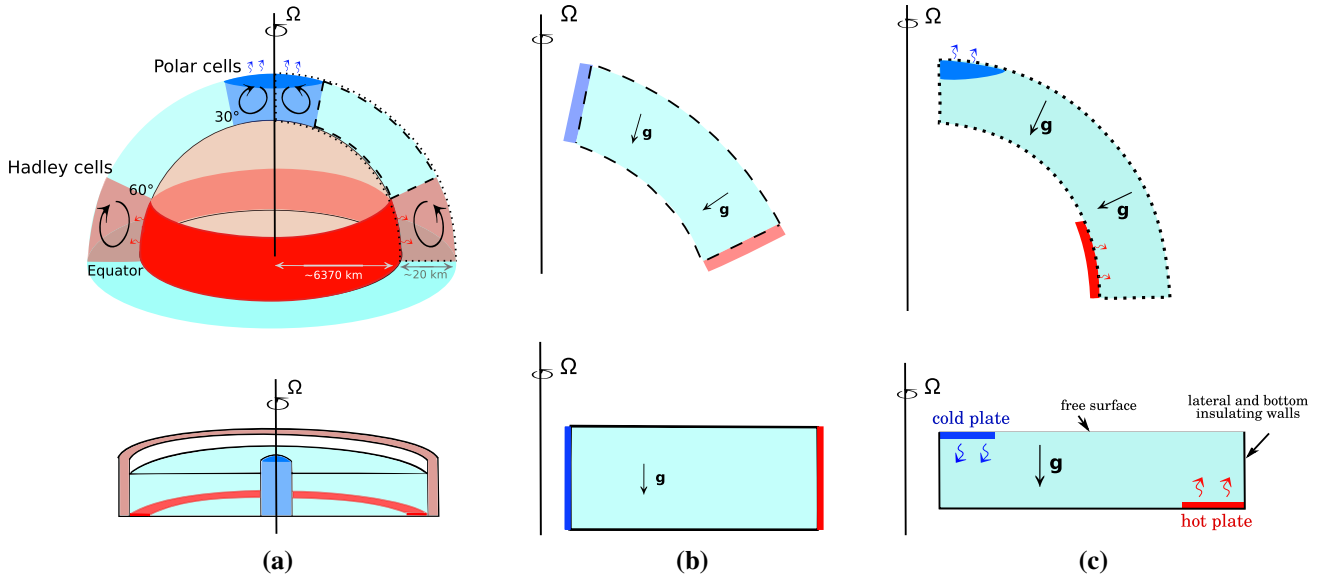

Fig. 1 **a** Sketch of a simplified structure of the global atmosphere and location of the dominant global thermal heat sinks and sources and its analogue in the laboratory in cylindrical configuration. **b**, **c** Schematic views of a section of mid-latitude atmosphere, as represented **b** in the classical annulus and **c** in the new annulus analogue, taking into account the heat sink in the upper atmosphere in the polar region and the heat source close to the ground in tropical regions. In each configuration sketched in 2b or 2c, the unwrapped rectangular shape obtained corresponds to one half *r*-*z* section of the experimental annular configuration. Axisymmetry with vertical axis is implicit and assumed near the inner vertical boundary near the heat sink region, as illustrated in **a**

providing the possibility of precise, reproducible experiments to test ideas and hypotheses.

In the spirit of this approach, the idealization of the mid-latitude atmosphere in the laboratory as a differentially-heated, rotating, cylindrical annulus (see Fig. 1a) originally proposed by Hide, has proved to be a prolific and productive analogue of many features of the atmospheric circulation (Hide 1958; Fowlis and Hide 1965; Hide et al. 1977; Read et al. 2014). By combining only the three essential physical ingredients forcing the atmosphere, i.e., gravity, rotation, and differential heating, the 'classical' thermally driven rotating annulus setup provides an experimental configuration that enables both large-scale overturning circulations and baroclinic instabilities to be studied and explored. It consists of an assembly on a rotating platform with a fluid contained between two upright, coaxial cylinders that are maintained at different temperatures, with thermally insulating, horizontal endwalls (see Fig. 1b) and reproduces fluid motions and baroclinic instabilities that transport heat from the equator, where solar heating of the surface is most intense, towards the cooler polar regions in the atmosphere. In addition, the latitudinal dependence of the Coriolis force (the so-called 'beta-effect') can also be reproduced by simply adding a conical topography at the bottom inside the annulus (e.g., Bastin and Read 1997).

Thus, this setup has proven to be a simple enough system to capture the fundamental physics and with enough complexity to represent nonlinear features and transition sequences to chaos similar to those of atmospheric dynamics (Hignett et al. 1985; Früh and Read 1997; Bastin and Read 1998; Read 2003; Von Larcher and Egbers 2005; Wordsworth et al. 2008; Vincze et al. 2014). It has also proved valuable as a tractable 'test bed' within which to test numerical codes and methods (Harlander et al. 2011; Vincze et al. 2015) as well as to benchmark statistical–dynamical analysis methods in widespread use in meteorology, such as data assimilation (Young and Read 2013). Moreover, it is even inspiring new experiments for studying non-terrestrial planetary atmosphere dynamics in the laboratory (Read et al. 2015; Yadav et al. 2016).

The classical annulus configuration, however, has some important limitations as an analogue of the mid-latitude atmosphere, an important aspect of which derives from its use of isothermal vertical boundaries to provide heating and cooling. This leads to an intense, boundary layer dominated, overturning circulation which imposes a strong constraint on the background stratification in the working fluid, and which, therefore, limits the possibility for internal instabilities to change this, even at large equilibrated amplitudes. In contrast, in the real atmosphere (see Fig. 1a, c), the effective heat source in the tropics is located mostly near the ground (through absorption of infrared radiation re-radiated from the solar-heated surface), while the heat sink is

predominantly located in the upper troposphere in the mid-latitudes and polar regions[1] (e.g., see Chan and Nigam 2009). The resulting circulation spontaneously partitions itself into a convectively unstable/neutral region in the tropics that interacts with a statically stable, baroclinic region at mid-latitudes that, despite being cooled from above, is statically stable.

Precisely *how* is heat passed from the convectively turbulent region in the tropics into the stably-stratified sub-tropics and mid-latitudes is still not well understood quantitatively. In particular, it is not clear what determines the characteristics of the observed vertical stratification in the mid-latitude atmosphere (its static stability, surface thermal contrast, and tropopause height) and more generally what are the dominant mechanisms for nonlinear equilibration of baroclinic and convective instabilities in the atmosphere (e.g., see Schneider 2006; Stone 2008 for reviews).

Diverse theoretical and numerical studies of stratified macroturbulence and equilibration processes have recently explored the possible role of baroclinic instabilities in acting to stabilise their own thermal environment (Zurita-Gotor and Lindzen 2007; Zurita-Gotor and Vallis 2009, 2010; Schneider and Walker 2006; Schneider 2006). The idea of a feedback between the baroclinic instability and the thermal stratification was originally formulated by Stone (1978). In his baroclinic adjustment theory, based on the two-layer quasi-geostrophic model (Phillips 1951), a rotating, stratified fluid may adjust the mean thermal structure to maintain a stably-stratified environment that is close to a marginally critical state for baroclinic instability (Stone 1978) with a criticality parameter,ξ, that equilibrates to $\xi \approx 1$. ξ is a measure of the isentropic slope and defined as (Zurita-Gotor and Vallis 2010),

$$\xi = -\frac{f}{\beta H}\frac{\partial_y \bar{\theta}}{\partial_z \bar{\theta}} \tag{1}$$

with $\bar{\theta}$ the mean potential temperature, $f \equiv 2\Omega \sin\phi$ (where ϕ is latitude) and β quantifies the (linearised) dependence of the coriolis force on latitude so that $f \simeq f_0 + \beta y$ with f_0 a constant. Recent studies, however, have disputed this analysis, since numerical simulations have shown that the two-layer model does not necessarily equilibrate to a value of $\xi \approx 1$ (e.g., Salmon 1978, 1980; Vallis 1988).

[1] The situation in the polar atmosphere is complicated by the non-gray nature of atmospheric radiative transfer, which also (amongst other things) allows the surface to cool directly by radiating to space as well as the atmosphere.

Nonlinear wave–wave interactions may play a significant role in determining whether the flow equilibrates to a marginally critical ($\xi \lesssim 1$) or supercritical ($\xi > 1$) state (Vallis 1988; Schneider and Walker 2006; Schneider 2006). Some evidence further suggests that wave–wave interactions may become spontaneously suppressed under some conditions (Schneider and Walker 2006; Schneider 2006), leading to marginally critical conditions and the absence of a large-scale turbulent energy cascade, although the detailed structure of the heat sources and sinks may also be important in determining ξ (Zurita-Gotor and Vallis 2009, 2010). Schneider (2004) further highlights that the inhibition of nonlinear eddy–eddy interactions offers an explanation for the historic success of linear and weakly nonlinear models of large-scale extratropical dynamics, but also rests on the postulate that the kinematic mixing properties of baroclinic eddies exhibit no essential vertical structure. The key point here is that this problem remains highly active and controversial, and laboratory experiments of the kind described here may provide some valuable new insights.

In this study, to explore the impact of changes to the forcing on such baroclinic equilibration processes and the criticality parameter, we have constructed a new laboratory analogue of atmospheric circulation with a rotating annulus that is convectively forced by *local* differential heating on *horizontal* boundaries. We aim, thereby, to relax some of the thermal constraints on background temperature gradients in the 'classical' annulus experiments to better represent qualitatively how the thermal structure of the atmosphere itself is maintained, with particular reference to the equilibration mechanisms of convective and baroclinic instabilities. Section 2 describes the characteristics of the new experimental apparatus. Validation of the setup and some preliminary results are presented in Sect. 3 and briefly discussed in Sect. 4.

2 Experimental setup

The new experimental configuration is inspired by the schematic model, as illustrated in Figs. 1c and 2. By unwrapping the spherical domain, this leads to the usual atmosphere-like cylindrical configuration, but where local differential heating at the horizontal boundaries is used to emulate the radiative heat sink in the upper atmosphere in the polar regions and the heat source near the ground in tropical regions. This allows the possibility of the formation of a statically stable (though baroclinically unstable) zone, sandwiched between convectively unstable regions over/underlying the heated or cooled boundaries (Wright et al. 2017) and permits a possible feedback of the resulting baroclinic instability onto the background stratification. Figure 2 illustrates the

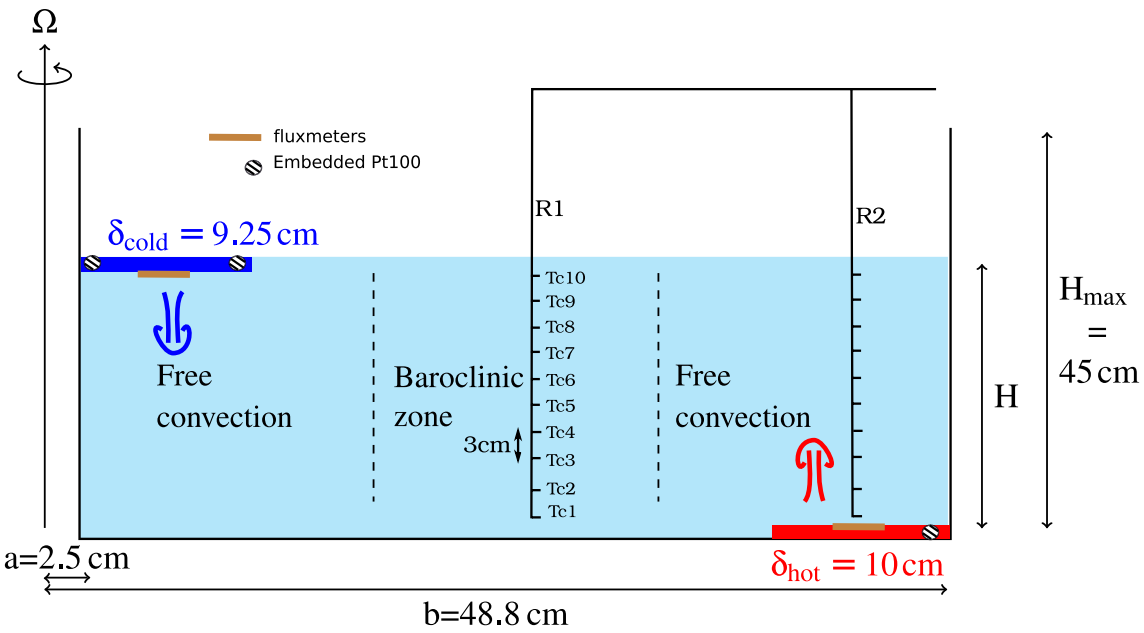

Fig. 2 Schematic cross section of half of the new annular experimental setup with local thermal heat source and heat sink horizontally and vertically displaced. 3 mm diameter rods instrumented with ten type T microthermocouples are introduced in the fluid to measure thermal stratification above the statically stable zone at mid-radius and centered above the heated external zone

experimental configuration, with the fluid contained within an annular channel between two upright, rigid, coaxial, thermally insulating cylinders and a flat (or conical), horizontal base, within which the outermost $\delta_{\text{hot}} = 10$ cm in radius is maintained with a constant heat flux and equilibrates at a corresponding temperature T_b, while for $r < b - 10$ cm, the lower boundary is thermally insulating (perspex material). The upper surface is free-slip except for the innermost $r \leq \delta_{\text{cold}} = 9.25$ cm, for which the temperature T_a is fixed, thanks to circulating water within the cold central plate and such that $T_b > T_a$. The whole system rotates uniformly about the axis of symmetry in an anticlockwise direction at angular velocity Ω up to 3.5 rad s^{-1}.

The global design and a view of the whole assembly of the new experimental setup are presented in Fig. 3. This shows the perspex tank of internal radius $b = 48.8$ cm, filled with water and including the aluminium circular ring of radial width 9.25 cm attached to a central 5 cm diameter cylindrical post (i.e., with inner annulus radius $a = 2.5$ cm) cooled with water circulated from an external water bath in the lab frame (see Fig. 3a) via a DSTI$^{\text{TM}}$ rotary union. Top-view cameras can be seen attached to the embedded rotating aluminium framework. The 10 cm wide, electrically heated, annular ring is composed of two aluminium plates, onto the lower face of each of which two flexible, plastic-coated Clarian$^{\text{TM}}$ heaters (each resistance $\approx 18 \pm 1\Omega$) are attached. All four heaters are connected in a parallel configuration to a 10A-35V TTI Thurlby Thandar TSX3510P power supply. Both the cold plate and the electrically heated annular plate are equipped with Captec$^{\text{TM}}$ heat fluxmeters and thermal probes, platinum resistance sensors and type T thermocouples, with watertight wire connections at the bottom of the tank (see Fig. 3c).

To monitor the temperature within the fluid and measure the thermal stratification, 3 mm diameter rods instrumented with ten type T microthermocouples have been introduced in a flexible way above the central (baroclinic) zone at mid-radius and above the heated external (convective) zone, as sketched in Fig. 2 and visible in Fig. 3a inside the tank. Calibration of the thermocouples was carried out independently by immersing the rods in the temperature-controlled reservoir of the chiller and using its built-in platinum resistance probe as a reference. As visible in Fig. 3a–c, an annular silver-coloured ring is located around the tank and consists of a series of white light LED arrays, collimated between two thin, aluminium plates to generate a 5 to 10 mm-thick horizontal white light sheet. On the shelf underneath the main turntable are located a remotely controlled computer, connected by a GPIB connection to the acquisition system for the thermal probes (a computer-controlled Agilent 34970A data logger unit with a 34901A card for measurements using 4-wire platinum resistance sensors and acquisition of voltages from fluxmeters, and a 34908A card for type T thermocouple measurements), and power supplies for the lights and annular heaters (see Fig. 3a). The data logger is set to acquire temperature measurements every 1 or 2 min in the general monitoring configuration and, depending on acquisitions, every 5 or 10 s in equilibrium phases.

Table 1 Range of parameters of presented experiments in the new locally forced thermally driven rotating annulus setup

Parameter	Symbol	Present range	Units
Rotation rate	Ω	0.01–1.1 (up to 3.5)	rad s^{-1}
Temperature difference	ΔT	$\approx 8-10$	K
Fluid properties at 20 °C (in the case of 17% glycerol solution)			
Density	ρ	1041–1045	kg m^{-3}
Thermal expansion coefficient	α	2.75×10^{-4}	K^{-1}
Kinematic viscosity	ν	1.71×10^{-6}	$m^2\ s^{-1}$
Thermal diffusivity	κ	1.28×10^{-7}	$m^2\ s^{-1}$
Geometry			
Inner radius	a	0.025	m
Outer radius	b	0.488	m
Horizontal scale	$L \equiv b - a$	0.463	m
Cold plate radial width	δ_{cold}	0.0925	m
Heat annular radial width	δ_{hot}	0.010	m
Mean fluid depth	H	0.30	m
Non-dimensional parameters			
Thermal Rossby number (Eq. (3))	Θ	2×10^{-2}–100	
Ekman number (Eq. (9))	E	5×10^{-6}–3×10^{-4}	
Taylor number (Eq. (5))	Ta	10^8–10^{12}	
Rayleigh number (Eq. (7))	Ra	3.4×10^{-9}	
Boundary layer thicknesses ratio (8))	P	[0.1–1]	
Prandtl number (Eq. (11))	σ	≈ 7 (water only) or 13.4 (water–glycerol solution)	
Aspect ratio (Eq. (10))	Γ	1.54	

The principal dimensionless parameters expected to govern the behaviour of the system are in common with the conventional rotating annulus experiment. Thus, the thermal Rossby number is a stability parameter comparing the characteristic velocity U_T of the thermally driven flow, consistent with the geostrophic thermal wind relation

$$_T \approx \frac{g\alpha H \Delta T}{\Omega L}, \tag{2}$$

with the velocity scale ΩL based on the rotation rate and the typical horizontal size of the tank $L = b - a$:

$$\Theta = \frac{U_T}{\Omega L} = \frac{g\alpha H \Delta T}{\Omega^2 L^2} \tag{3}$$

with α the thermal expansion coefficient and ΔT the temperature difference between the plates (see Table 1).

The thermal Rossby number Θ can be related to the Burger number:

$$\text{Bu} = \left(\frac{NH}{2\Omega L}\right)^2 = \left(\frac{R_\text{d}}{L}\right)^2, \tag{4}$$

where N is the buoyancy frequency $N^2 = -(g/\rho)\partial\rho/\partial z$, via a factor proportional to the mean slope of the isotherms (and isopycnals) $\sim \Delta T_{\text{horiz}}/\Delta T_{\text{vert}}$. Linked to the vertical static stability, Bu represent the ratio of $R_\text{d} = NH/(2\Omega)$, the Rossby deformation radius (a typical length scale of baroclinic motion) to the scale of the domain L, and is a key parameter determining the onset of baroclinic instability (Hide and Mason 1975).

The importance of viscous forces compared to Coriolis effects is described by the Taylor number in the form deduced by Fowlis and Hide (1965):

$$\text{Ta} = \frac{4\Omega^2 L^5}{H\nu^2} \approx \left(\frac{\text{Coriolis acceleration}}{\text{friction force/unit mass}}\right)^2 \tag{5}$$

where symbols are as defined in Table 1.

Following Hignett et al. (1981), Read (1986), King et al. (2009) and Read et al. (2014), we anticipate that a significant parameter associated with the thermal structure of the system will be the squared ratio of the characteristic length scales of the buoyancy-driven thermal boundary layer (without rotation) and the Ekman layers. Assuming that the thermal boundary layer length scale $\ell_T = H/(2\text{Nu}) \sim H\text{Ra}^{-\gamma}$, where Nu is the Nusselt number characterising the efficiency of the heat transfer in the fluid in comparison with pure conduction

$$\text{Nu} = \frac{Q_\text{tot}}{Q_\text{conductive}}, \tag{6}$$

Ra is the Rayleigh number

Fig. 3 **a** Global view of the experimental configuration. The chiller used for the water circulation in the central cold plate can be seen on the left below the turntable control unit in *gray*. The two vertical rods inside the tank and their corresponding light-brown electrical wires connected to the ten thermocouples can be distinguished on the left-hand side of the tank. **b** 3D zoomed view of the design of the new setup with the electrically heated annular ring at the bottom of the tank shown in *red* and the cooling imposed through a circular disk at the centre of the tank at the upper surface in *blue* (with cold water circulation). **c** Top-view of the convection chamber showing the cold plate and aluminium annular ring instrumented with platinum resistance sensors and two heat fluxmeters (*orange squares* at the *bottom*) fixed onto the outer heated ring

$$\mathrm{Ra} = \frac{g\alpha\Delta T H^3}{\nu\kappa}, \tag{7}$$

and γ is an exponent that depends on the convective regime (e.g., see Chillà and Schumacher 2012), the boundary layer ratio parameter may be defined as

$$P = \left(\frac{\ell_T}{\ell_E}\right)^2 \propto \mathrm{Ra}^{-2\gamma} E^{-1}, \tag{8}$$

where $\ell_E = HE^{1/2}$ is the Ekman layer thickness with E the Ekman number:

$$E = \frac{\nu}{\Omega H^2}; \tag{9}$$

P is, therefore, directly proportional to Ω.

Other intrinsic parameters are determined once geometry and working fluid are chosen: the aspect ratio:

$$\Gamma = \frac{L}{H}, \tag{10}$$

the Prandtl number:

$$\sigma = \frac{\nu}{\kappa}, \tag{11}$$

which compares viscous and thermal diffusivities.

Experiments presented in this paper have been carried out in a flat-bottom configuration and with a 30 cm depth of either pure water or, to increase the density, a 17% solution by volume of glycerol and water (which also changed the viscosity and Prandtl number).

The two heaters were typically energised with an electrical power of 206W for the annulus, while the command temperature of the bath for the water circulation was set to 14 °C and air-conditioning was set to 21 °C in the room. This led to a maximum effective $\Delta T \approx 8$ to 10 °C

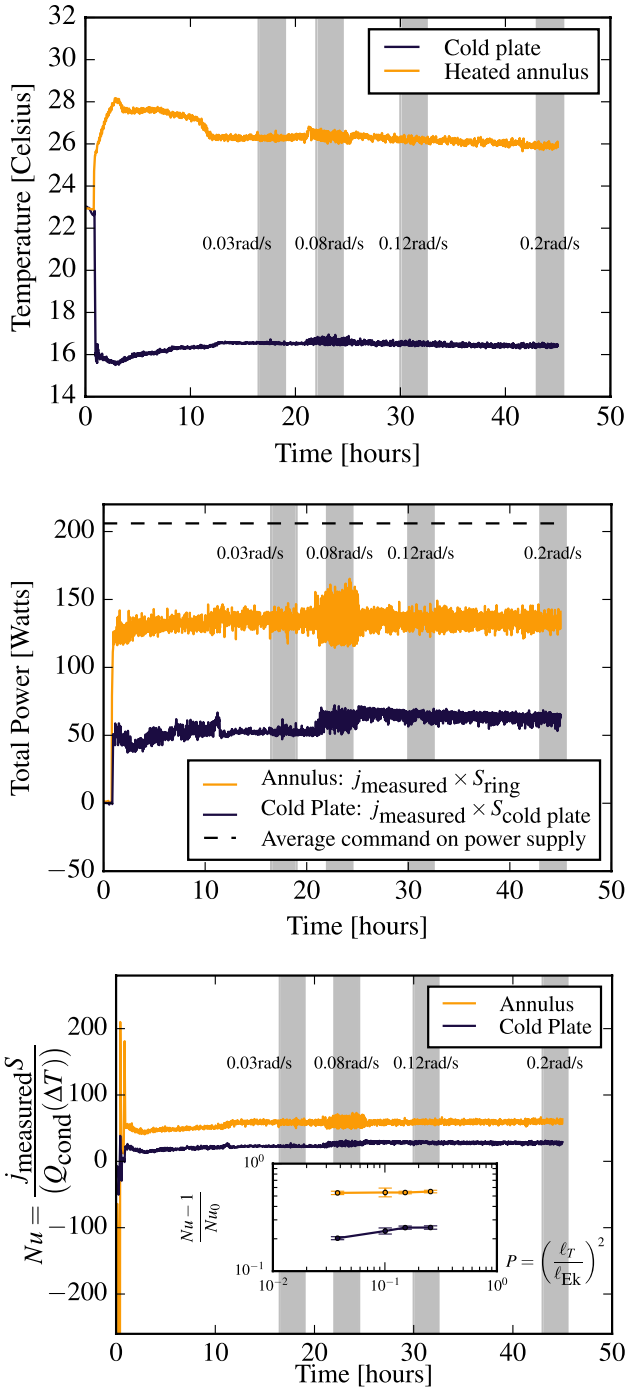

Fig. 4 Evolution of temperature measured with Pt100 platinum resistance sensors **a**, total power **b**, and Nusselt number through plates **c** for the glycerol and particles experiment. The *dashed line* in **b** shows the electrical input power. *Inset* in **c** corresponding evolution of the normalized Péclet number $(\text{Nu}-1)/\text{Nu}_0$ with P, squared ratio of non-rotating thermal boundary layer thickness and Ekman boundary layer thickness. Normalization is performed with the non-rotating Nusselt number Nu_0 estimated with a 2/7 scaling law following Wright et al. (2017)'s results, [see also Shraiman and Siggia (1990) and review by Chillà and Schumacher (2012)]. *Errors bars* shown are illustrating standard deviation on the averaging period at a given rotating rate

between the cold plate and the aluminium annular ring at equilibrium, as illustrated in Fig. 4. This was associated with a measured total power from the heated ring and into the cold plate of around 150 and 50 W, respectively (Fig. 4b). The 100 W loss is consistent with the average $T_{\text{bulk}} \approx 23-25$ °C being larger than the temperature of the air-conditioned room (21 °C). Although the total power from the cold plate was smaller than the one from the heated annulus, the flux (in W/m^2) through the cold plate is found, as expected, to be larger than through the annulus, since the whole annulus surface area ($S \approx 0.27\,\text{m}^2$) is larger than that of the cold plate ($S \approx 0.041\,\text{m}^2$).

The whole system rotated uniformly about the axis of symmetry at angular velocity $\Omega = 0.03$–1.1 rad s^{-1} in the current series of experiments. A summary of the values and ranges of the main parameters for the current experiments is listed in Table 1. After the first day or two of equilibration, changes in rotation rate were carried out and the system was allowed to relax to a new equilibrated dynamical regime for 1 h or more and thermally monitored before image acquisition.

In experiments using pure water, an exploration of the different regimes was performed by injecting a concentrated solution of fluoresceine dye to highlight vortices and other flow features, while in the water–glycerol experiments, 355–500 μm Pliolite particles matching the density of the solution ($\approx 1.043 \times 10^3$ kg m^{-3}) were suspended in the fluid and illuminated by the LED light sheet to trace the flow. Images were acquired with a DFK 31BF03 *Imaging Source* firewire camera (resolution 1024 × 768) and an ethernet AVT Manta 609B camera (resolution 2752 × 2206) within the rotating frame of reference at a frame rate of 1 fps. In experiments with particles, streaklines were produced by superposing 20 or 50 images together in a given equilibrated regime. In addition, an FLIR i50 thermal imaging camera (resolution 240 × 320) was used to image the temperature variations across the surface of the water.

3 Results

3.1 Thermal structure

As explained in introduction and sketched in Fig. 2a and as shown in numerical simulations of axisymmetric flow 2D regimes of the same system (see Fig. 5 and Wright et al. 2017), the formation of a statically stable though baroclinically unstable zone in the central area is expected at equilibrium, sandwiched between convectively unstable regions over/underlying the heated or cooled boundaries.

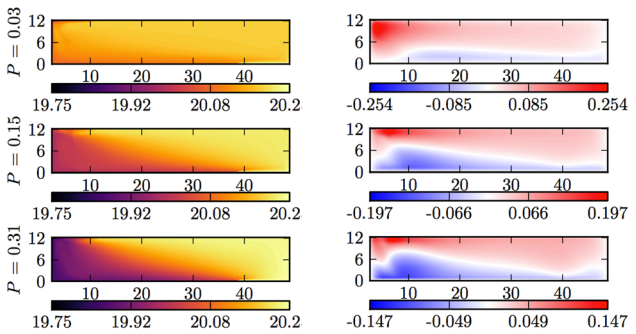

Fig. 5 Temperature (*left*) and azimuthal velocity (*right*) fields of 2D axisymmetric flows simulations (Wright et al. 2017) for P ratio in the range [0.1–1] [extract reproduced from data of Wright et al. (2017)]

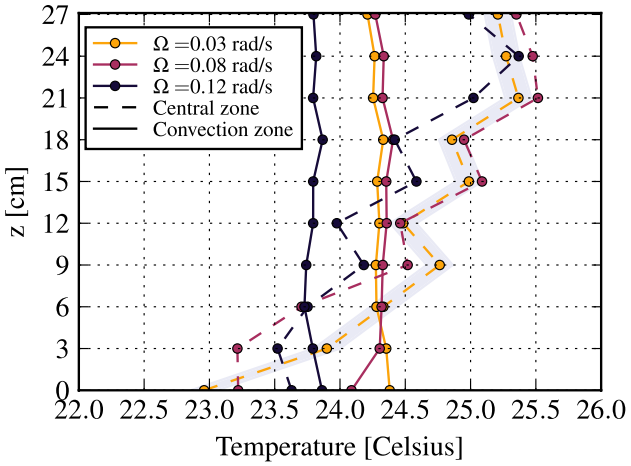

Fig. 6 Measurements of vertical temperature profiles for the mid-radius zone and the zone above the heated ring averaged for 2.5 h in the glycerol-solution experiment showing, respectively, statically stable baroclinic zone and isothermal features. *Gray* area (shown only on one profile in the central zone for clarity) is the estimated ±0.1 °C uncertainty. The measurement of the global stratification within the central zone (avoiding the two topmost temperature points) allows an estimation of the associated Burger numbers (defined in Eq. 4) of Bu $\approx [3.6, 0.65, 0.15] \pm 0.1$ for the corresponding $\Omega[\mathrm{rad\,s^{-1}}] = [0.03, 0.08, 0.12]$

When background rotation is significant, two regimes were identified as a function of the rotation rate and classified as a function of P, the ratio of (non-rotating) thermal boundary layer to Ekman boundary layer thicknesses (Read 1986; Read et al. 2014; Wright et al. 2017). An (r, z) cross section of the temperature field from axisymmetric numerical simulations by Wright et al. (2017) of the similar configuration as the current experiment is illustrated in Fig. 5 for the range P [0.1–1]. A secondary density current that flows beneath the heat sink, down the side of the inner cylinder and along the base towards the heat source, was found under very weak rotation conditions (Wright et al. 2017). For weak rotation (defined as $0.05 \lesssim P \lesssim 0.2$), this is replaced by a more uniform thermal gradient, with almost vertical isotherms close to the inner and outer cylinders, confined to Stewartson layers on the vertical boundaries, in association with a developing vertical shear in the azimuthal velocity (see Fig. 5 and Wright et al. 2017).

For moderate rotation rates with P of order or above unity ($0.2 \lesssim P \lesssim 2$), the thicknesses of the thermal boundary layer and the Ekman layer are comparable. Free convection then results in well-mixed, approximately isothermal, regions above and below the heat source and sink, respectively. Sandwiched between these two convective zones there emerges a stably-stratified baroclinic region with approximately uniformly sloping isotherms. In association with the horizontal temperature gradient obtained within the tank, a strong vertical shear of the azimuthal velocity is now seen to have developed, as consistent with the geostrophic thermal wind balance.

This thermal structure found in the 2D simulations (Wright et al. 2017) was approximately validated in experiments using a water–glycerol solution, as shown in the time-averaged temperature profiles in Fig. 6, which were taken for different rotation rates at equilibrium (indicated by the shaded zones in the time series shown in Fig. 11): an overall stable stratification tendency is found in the central region, while an almost isothermal profile is indeed measured above the heated annular ring.

During the transition towards thermal equilibrium (before 15 h, not shown), the temperature measured by thermocouples at the bottom of probe R2 (very close to the heated ring near the external walls) rapidly rises as expected, while thermocouples at the top first of R2 become colder and then equilibrate to an almost isothermal configuration after 15 h. In the mean time, thermocouples on probe R1 in the central zone at mid-radius reveal an equilibration towards a final statically stable configuration, as confirmed by time-averaged temperature profiles in Fig. 6. As the squared ratio of thermal boundary layer to Ekman boundary layer thicknesses, P, is estimated to be below or around unity for the current experiments (see also values in Fig. 4c, inset), these thermometric results are consistent with the global picture of two almost well-mixed near-isothermal convection zones separated by a statically stable baroclinic zone as seen in simulations over the same range of P ratio (see Fig. 5).

The thermal structure differs somewhat in the case of experiments using a water-only solution and dye visualisation (see Figs. 7, 8), but a statically stable interval is still present in the lower part of the profiles, merging into a more isothermal section in the upper part of the profile. This may be due to convection processes still at play as the flow gradually evolves towards equilibrium (given a shorter dwell time at each rotating rate) or alternatively

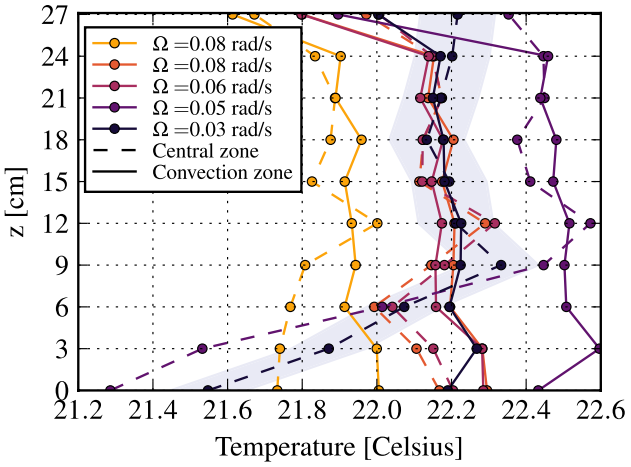

Fig. 7 Measurements of vertical temperature profiles for the mid-radius zone and the zone above the heated ring averaged for 1 h in the water-only experiment with $T_{\text{command cold water bath}} = 14$ °C and input power in heated ring = 206 W. *Gray* area (shown only on one profile in the central zone for clarity) is the estimated ±0.1 °C incertainty

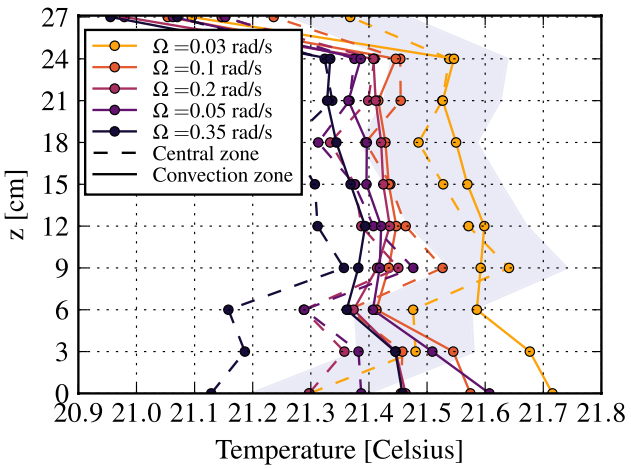

Fig. 8 Measurements of vertical temperature profiles for the mid-radius zone and the zone above the heated ring averaged for 20 min in the water-only experiment with $T_{\text{command cold water bath}} = 18$ °C and input power in heated ring = 97.5 W. *Gray* area (shown only on one profile in the central zone for clarity) is the estimated ±0.1 °C incertainty

may have been the result of evaporation and wind stress processes at the surface due to there having been no enclosure around the tank at that time (in contrast to the water–glycerol experiments conducted afterwards). We estimated the power lost at the free surface due to evaporation ($P_{\text{evapo}} = L_h \rho \mathrm{d}V/\mathrm{d}t$, where L_h is the water latent heat and $\mathrm{d}V/\mathrm{d}t$ the volumetric debit) by performing a rough monitoring of the decrease in time of the water level along the depth of the cold plate in water-only experiments. The power lost via evaporation process was found to be in the range 50–80 W, so not negligible compared to the power through the cold plate. This effect is likely to be still present in the glycerol case and temperature profiles in Fig. 6 in the mid-radius central zone also suggest the formation of a mixed layer in the uppermost few centimeters beneath the surface, in contrast to what is found in numerical simulations, where a rigid-lid boundary was used. However, this effect seems somewhat reduced, partly due to the physical properties of the mixture, or more likely mainly due to the enclosure of the whole setup with thick black fabric. Fluctuations can be seen in the interior of the same profiles within this central zone, however, which should be investigated in further experiments.

Thus, at least some of these observed differences between pure water and glycerol mixture experiments in temperature profiles are likely due to evaporation effects. This illustrates the well-known imperative in rotating experiments with a free surface to reduce air exchange between air above the tank with the air in the room using thick curtains or panels or the use of rigid-lid experimental configurations, to prevent potentially non-negligible evaporation and wind stress effects. In the present case, the flux (in W/m^2) through the cold plate is much larger than through the free surface. Since the free surface is 17 times larger than the cold plate area, however, convective plumes can be expected to be more intense underneath the cold plate than the free surface.

3.2 Heat transport

The use of fluxmeters on the cold plate and on the heater ring allows us to estimate the Nusselt number, as illustrated in Fig. 4c, for the glycerol experiments. For estimating the conductive power Q_{cond} in the denominator of the measured Nusselt number in in Fig. 4c, the coefficient of proportionality of Q_{cond} with ΔT was retrieved from numerical calculation solving the steady conduction equation for the same control and geometrical parameters. Then, the heat transport efficiency is written in the form of normalized Péclet value $(\mathrm{Nu} - 1)/\mathrm{Nu}_0$. The Péclet number associated with the annular heated ring is found fixed, while on the cold plate, it is found that it rises with the P ratio, i.e.,with Ω (Fig. 4c). Such two Nusselt number measurements associated with fluxmeters signals on each plate normally give two estimates of the same quantity. However, in reality, the power budget is distributed as $P_{\text{hot plate}} = P_{\text{cold plate}} + P_{\text{free surface}} + P_{\text{walls}}$, with lateral conduction through perspex walls P_{walls} likely to be negligible compared to the others, given the small difference between the bulk temperature and the room temperature. $P_{\text{free surface}}$ is likely dominated by evaporation and whose value estimated above is consistent with this global budget given the values of power measured through the heated

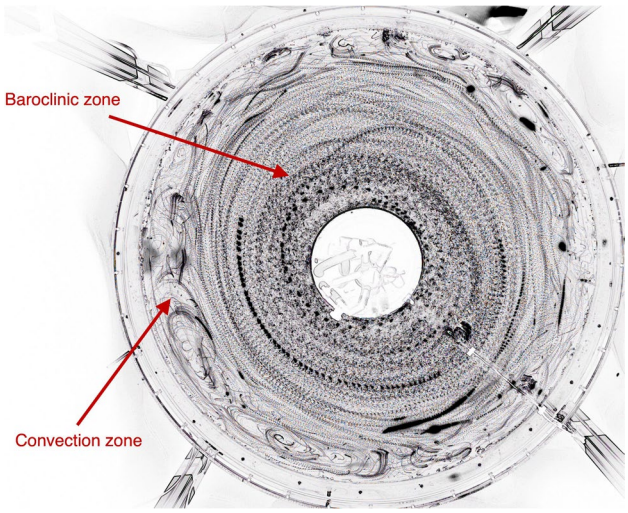

Fig. 9 Dynamical regime for $\Omega = 0.08\,\mathrm{rad\,s^{-1}}$ in case of mixed glycerol–water solution experiment illustrated with streak lines of particles and showing the 'sandwich' configuration of low-order wavenumber baroclinic zone with convection zone (see also supplementary material Movie 3)

annulus and cold plate. Therefore, the Nusselt number retrieved from the cold plate seems the more relevant estimate to better reflect the transverse thermal efficiency and the different flow dynamical regimes depending on rotating rate than the Nusselt based on the heated annulus measurements. Even if the configuration is fully 3D here and with the presence of baroclinic instabilities, in contrast to numerical axisymmetric 2D simulations, it turns out that a similar increase of normalized Péclet number from the cold plate as a function of P was found by Wright et al. (2017) in the [0.04–0.2] range.

3.3 Horizontal flow

The flow configuration anticipated from the numerical simulations of Wright et al. (2017), of a baroclinic zone sandwiched between two convection zones, is further validated in horizontal streakline features, as illustrated in Figs. 9 and 10 (and the Online Resource video, for example, in the 0.08 and 0.12 rad s^{-1} cases; Movies 3 and 4). A clear separation can be noticed between the mid-radius zone, with the large amplitude baroclinic wave (Fig. 9 reveals a non-axisymmetric pattern consistent with baroclinic mode 1 or even an elliptic pattern corresponding to baroclinic mode 2), and a zone in an outer annular strip near the external wall presenting small-scale features likely to be remnants of the Rayleigh–Bénard convection plumes in that zone. Even in snapshots exhibiting a larger amplitude of baroclinic wave at $\Omega = 0.12\,\mathrm{rad\,s^{-1}}$, the meandering jet does not seem to reach the outer cylinder. This new experimental setup, therefore, offers the capability of exploring the properties of fully developed baroclinic instabilities with minimal interference from sidewall boundaries.

At low rotation rates, the experimental flows observed are consistent with the structure of the azimuthal velocity predicted by 2D axisymmetric simulations (see cases $P = 0.03$ and $P = 0.15$ in Fig. 5 and Wright et al. 2017). The occurrence of higher values of azimuthal velocity underneath and near the inner cold plate than at larger radii is confirmed for the $\Omega = 0.03$ and $0.08\,\mathrm{rad\,s^{-1}}$ cases, as illustrated in the video of a close-up view of dye experiments (e.g., Movie 1 in the supplementary Online Resource) and in streakline movies (Movies 2–3 in supplementary Online Resource). This occurrence of an intense 'polar vortex' is particularly interesting as this characteristic has been suggested as a significant dynamical feature in slowly rotating planetary atmospheres such as on Titan (Lebonnois et al. 2012) and Venus.

3.4 Baroclinic instability

In the range of rotation rates and temperature differences used, it is expected that isopycnals in the statically stable region near mid-radius would be quite strongly sloped, allowing baroclinic instabilities to be able to grow. Figure 10 shows examples of typical observations of flow patterns found in the fluid, illustrated with passive dye tracer images (after substraction and/or inversion of the image), particle streaklines and infrared thermographic camera images. Indeed, several modes of baroclinic instability were observed, from low-order, regular, azimuthal wave modes at small angular velocities to irregular and turbulent motions with small, chaotic vortices at higher rotation rates, as illustrated in Fig. 10 and in movies 2–5 in the supplementary Online Resource. For $\Omega = 0.12\,\mathrm{rad\,s^{-1}}$, the baroclinic wave is particularly highly developed and presents an almost steady mode 3 associated with a measured Burger number Bu = 0.15. Thus, the onset of strong baroclinic waves is found just above 0.08 rad s^{-1} which corresponds to Bu = 0.65 (see Figs. 6, 10), which is approximately consistent with the Eady criterion (see Hide and Mason (1975), with an instability threshold at Bu = 0.581). The evidence of weak instability for 0.03 rad s^{-1} up to 0.08 rad s^{-1} (Bu = 3.6 and 0.65, respectively) suggests the presence of instability beyond the Eady cutoff. This is also consistent with the zone of weak waves found by Hignett et al. (1985) (see symbol w in Fig. 10) suggesting a possible vertical confinement or surface intensification of baroclinic waves (Hide and Mason 1978; Jonas 1980). This will be investigated in future work. Nonlinear amplitude vacillation features, similar to those found in classical rotating annulus experiments (e.g., Früh and Read 1997), were also observed. Thus, it was observed, e.g., at rotation rate 0.12 rad s^{-1}, that a baroclinic mode with the initial

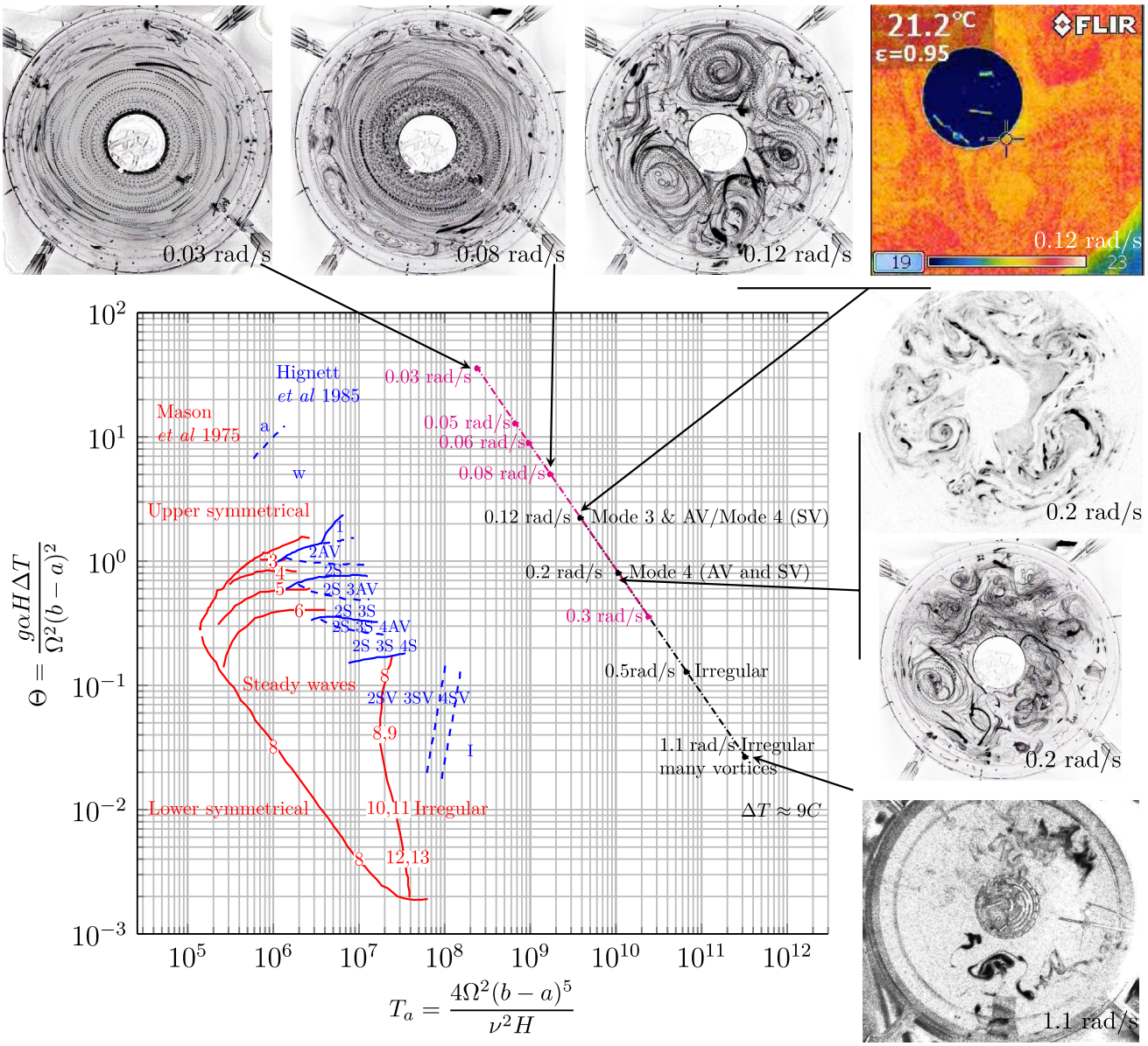

Fig. 10 Regime diagram as a function of Taylor number and thermal Rossby number. *Black* and *magenta points* correspond to two separate experimental runs and show the experimental dynamical regimes explored. Previous results from Mason (1975) and Hignett et al. (1985) in red and *blue lines* have been plotted for comparison. *Numbers* represent mode wavenumber and added symbols that follow original annotations in Hignett et al. (1985) with a, axisymmetric; *w* weak waves, *S* steady waves, *AV* amplitude vacillation, *SV* shape vacillation, *I* irregular. See also movies in supplementary material

wavenumber 3 was found to evolve to a mode 4 (i.e., suggesting a form of nonlinear wavenumber vacillation). Other realizations at a similar rotation rate revealed an evolution of a mode 3 with varying amplitude (i.e., amplitude vacillation), as illustrated in supplementary material Movie 4.

In the same way, with a zoomed-in view of temperature time series from the thermocouple probes in the central zone at mid-radius, Fig. 11 also shows oscillatory patterns that reveal a slow drift of the lowest wavenumber components around the tank ($\tau_{\text{drift}} \approx 55\text{min}$) for $\Omega = 0.03\,\text{rad}\,\text{s}^{-1}$ (see also Fig. 12 for a closer view and Fourier analysis of it) and more complex, nonlinear baroclinic oscillations at higher rotation rates. A deeper analysis of these features is beyond the scope of this paper and will necessitate longer duration of data acquisition at a given equilibrium state for each rotation rate in future experiments; this will be presented elsewhere.

Finally, we compare our results with previous observations of baroclinic modes with the classical rotating annulus configuration. Figure 10 shows the location of the different observed modes in a *Ta*-Θ regime diagram on which the locations of various dynamical regimes

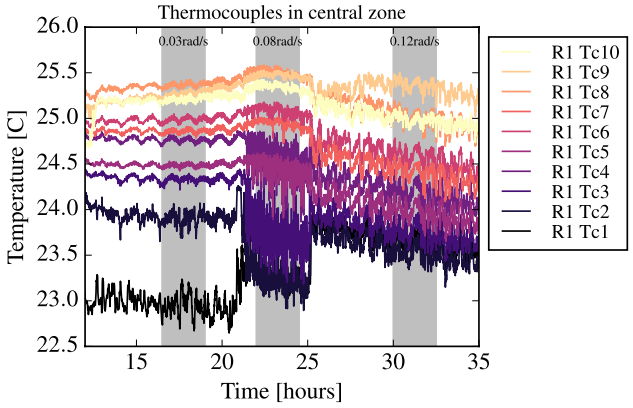

Fig. 11 Time series of thermocouples probes in the central zone at mid-radius for equilibrated state for the different rotating rates

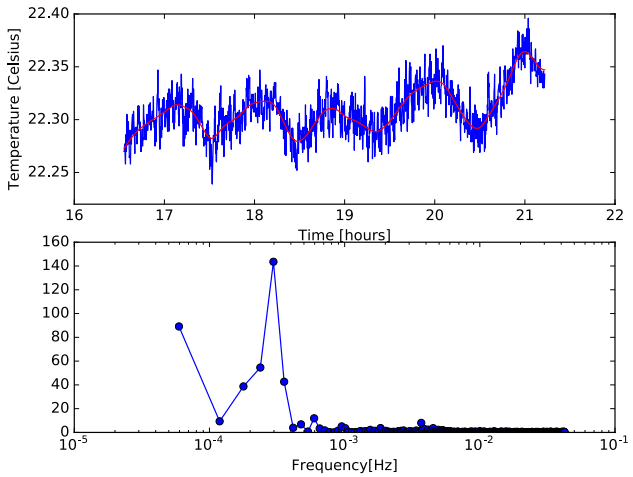

Fig. 12 **a** Zoomed view of time series of one of the thermocouple located in the mid-radius statically stable baroclinic zone for a rotating rate of 0.03 rad s^{-1} with the same high-frequency filtered signal superimposed. **b** Fourier plot associated with the visible $T = 55$ min drift

from previous thermally driven annulus experiments using the classical configuration (Mason 1975; Hignett et al. 1985) are superimposed. This indicates a reasonably good agreement with our experiments in the regions of different wave regimes, between the new locally forced atmosphere-like configuration compared to the classic rotating annulus case.

4 Conclusion

A new atmosphere-like experiment has been designed in the form of a local, convectively forced, thermally driven, wide rotating annulus to emulate more effectively than in previous experimental studies the distribution of local heat sinks in the upper troposphere of the Earth in the polar regions and a heat source near the ground associated with strong convection in tropical regions. The first experiments with this new "baroclinic sandwich" setup exhibit the thermal structure in the (r, z) cross plane anticipated from the 2D numerical simulations of Wright et al. (2017), as well as a fast 'polar vortex' and the confirmation of coexisting baroclinic and convection zones in the flow structure. This validates this new experimental setup as a tool to study equilibration processes with coexisting baroclinic and convective instabilities in a form highly relevant to what occurs in a planetary atmosphere such as the Earth's.

Baroclinic instability wave modes are found to grow and equilibrate, in broad agreement with previous results in the more classical annular configuration, with similar zonal wavenumbers and vacillation behaviour. Future work will include the addition of a sloping bottom to take into account in the laboratory effects equivalent to lateral variations of the Coriolis parameter. Particle image velocimetry experiments will also then allow us to gain quantitative insights into the nonlinear baroclinic equilibration processes on the beta plane, as well as into the geostrophic turbulence regime, to help understand the peculiar characteristics and dynamics of a mid-latitude Earth-like atmosphere.

Acknowledgements The authors acknowledge support for this work by UK Engineering and Physical Sciences research Council with EPSRC grant EP/K029428/1. The authors are grateful to Bob Watkins and Andy Clack from Atmospheric, Oceanic & Planetary Physics, Oxford for their support during the experimental design. We credit Sylvie Su with the initial version of sketches of Fig. 1.

References

Bastin M, Read P (1998) Experiments on the structure of baroclinic waves and zonal jets in an internally heated, rotating, cylinder of fluid. Phys Fluids (1994-present) 10(2):374–389. doi:10.1063/1.869530

Bastin ME, Read PL (1997) A laboratory study of baroclinic waves and turbulence in an internally heated rotating fluid annulus with sloping endwalls. J Fluid Mech 339:173–198. doi:10.1017/S0022112097005259

Chan SC, Nigam S (2009) Residual diagnosis of diabatic heating from era-40 and ncep reanalyses: Intercomparisons with trmm. J Clim 22(2):414–428. doi:10.1175/2008JCLI2417.1

Chillà F, Schumacher J (2012) New perspectives in turbulent Rayleigh–Bénard convection. Eur Phys J E 35(7):1–25. doi:10.1140/epje/i2012-12058-1

Fowlis W, Hide R (1965) Thermal convection in a rotating annulus of liquid: effect of viscosity on the transition between axisymmetric and non-axisymmetric flow regimes. J Atmos Sci 22(5):541–558. doi:10.1175/1520-0469(1965) 022<0541:TCIARA>2.0.CO;2

Früh WG, Read P (1997) Wave interactions and the transition to chaos of baroclinic waves in a thermally driven rotating annulus. Philos Trans R Soc Lond A Math Phys Eng Sci 355(1722):101–153. doi:10.1098/rsta.1997.0003

Harlander U, von Larcher T, Wang Y, Egbers C (2011) Piv-and ldv-measurements of baroclinic wave interactions in a thermally driven rotating annulus. Exp Fluids 51(1):37–49. doi:10.1007/s00348-009-0792-5

Hide R (1958) An experimental study of thermal convection in a rotating liquid. Philos Trans R Soc Lond A Math Phys Eng Sci 250(983):441–478. doi:10.1098/rsta.1958.0004

Hide R, Mason P (1975) Sloping convection in a rotating fluid. Adv Phys 24(1):47–100

Hide R, Mason P (1978) On the transition between axisymmetric and non-axisymmetric flow in a rotating liquid annulus subject to a horizontal temperature gradient: Hysteresis effects at moderate taylor number and baroclinic waves beyond the eady cut-off at high taylor number. Geophys Astrophys Fluid Dyn 10(1):121–156

Hide R, Mason P, Plumb R (1977) Thermal convection in a rotating fluid subject to a horizontal temperature gradient: spatial and temporal characteristics of fully developed baroclinic waves. J Atmos Sci 34(6):930–950. doi:10.1175/1520-0469(1977) 034<0930:TCIARF>2.0.CO;2

Hignett BP, White A, Carter R, Jackson W, Small R (1985) A comparison of laboratory measurements and numerical simulations of baroclinic wave flows in a rotating cylindrical annulus. Q J R Meteorol Soc 111(467):131–154. doi:10.1002/qj.49711146705

Hignett P, Ibbetson A, Killworth PD (1981) On rotating thermal convection driven by non-uniform heating from below. J Fluid Mech 109:161–187. doi:10.1017/S0022112081000992

Jonas P (1980) Laboratory experiments and numerical calculations of baroclinic waves resulting from potential vorticity gradients at low taylor number. Geophys Astrophys Fluid Dyn 15(1):297–315

King EM, Stellmach S, Noir J, Hansen U, Aurnou JM (2009) Boundary layer control of rotating convection systems. Nature 457(7227):301–304. doi:10.1038/nature07647

Lebonnois S, Burgalat J, Rannou P, Charnay B (2012) Titan global climate model: A new 3-dimensional version of the ipsl titan gcm. Icarus 218(1):707–722

Mason P (1975) Baroclinic waves in a container with sloping end walls. Philos Trans R Soc Lond A Math Phys Eng Sci 278(1284):397–445. doi:10.1098/rsta.1975.0032

Phillips NA (1951) A simple three-dimensional model for the study of large-scale extratropical flow patterns. J Meteorol 8(6):381–394. doi:10.1175/1520-0469(1951) 008<0381:ASTDMF>2.0.CO;2

Read P, Jacoby T, Rogberg P, Wordsworth R, Yamazaki Y, Miki-Yamazaki K, Young R, Sommeria J, Didelle H, Viboud S (2015) An experimental study of multiple zonal jet formation in rotating, thermally driven convective flows on a topographic beta-plane. Phys Fluids (1994-present) 27(8):085–111

Read PL (1986) Regimes of axisymmetric flow in an internally heated rotating fluid. J Fluid Mech 168:255–289. doi:10.1017/S002211208600037X

Read PL (2003) A combined laboratory and numerical study of heat transport by baroclinic eddies and axisymmetric flows. J Fluid Mech 489:301–323. doi:10.1017/S002211200300524X

Read PL, Pérez EP, Moroz IM, Young RMB (2014) General circulation of planetary atmospheres. John Wiley & Sons, Inc, pp 7–44. doi:10.1002/9781118856024.ch1

Salmon R (1978) Two-layer quasi-geostrophic turbulence in a simple special case. Geophys Astrophys Fluid Dyn 10(1):25–52. doi:10.1080/03091927808242628

Salmon R (1980) Baroclinic instability and geostrophic turbulence. Geophys Astrophys Fluid Dyn 15(1):167–211. doi:10.1080/03091928008241178

Schneider T (2004) The tropopause and the thermal stratification in the extratropics of a dry atmosphere. J Atmos Sci 61(12):1317–1340. doi:10.1175/1520-0469(2004) 061<1317:TTATTS>2.0.CO;2

Schneider T (2006) The general circulation of the atmosphere. Annu Rev Earth Planet Sci 34:655–688. doi:10.1146/annurev.earth.34.031405.125144

Schneider T, Walker CC (2006) Self-organization of atmospheric macroturbulence into critical states of weak nonlinear eddy–eddy interactions. J Atmos Sci 63(6):1569–1586. doi:10.1175/JAS3699.1

Shraiman BI, Siggia ED (1990) Heat transport in high-rayleigh-number convection. Phys Rev A 42:3650–3653

Stone PH (1978) Baroclinic adjustment. J Atmos Sci 35(4):561–571. doi:10.1175/1520-0469(1978) 035<0561:BA>2.0.CO;2

Stone PH (2008) The atmospheric general circulation: some unresolved issues. Dyn Atmos Oceans 44(3):244–250. doi:10.1016/j.dynatmoce.2007.03.002

Vallis G (1988) Numerical studies of eddy transport properties in eddy-resolving and parametrized models. Q J R Meteorol Soc 114(479):183–204. doi:10.1002/qj.49711447910

Vincze M, Harlander U, von Larcher T, Egbers C (2014) An experimental study of regime transitions in a differentially heated baroclinic annulus with flat and sloping bottom topographies. Nonlinear Process Geophys 21(1):237–250. doi:10.5194/npg-21-237-2014

Vincze M, Borchert S, Achatz U, von Larcher T, Baumann M, Liersch C, Remmler S, Beck T, Alexandrov KD, Egbers C, Fröhlich J, Heuveline V, Hickel S, Harlander U (2015) Benchmarking in a rotating annulus: a comparative experimental and numerical study of baroclinic wave dynamics. Meteorologische Zeitschrift 23(6):611–635. doi:10.1127/metz/2014/0600

Von Larcher T, Egbers C (2005) Experiments on transitions of baroclinic waves in a differentially heated rotating annulus. Nonlinear Process Geophys 12(6):1033–1041. doi:10.5194/npg-12-1033-2005

Wordsworth R, Read P, Yamazaki Y (2008) Turbulence, waves, and jets in a differentially heated rotating annulus experiment. Phys Fluids (1994-present) 20(12):126–602. doi:10.1063/1.2990042

Wright S, Su S, Scolan H, Young R, Read P (2017) Regimes of axisymmetric flow and scaling laws in a rotating annulus with local convective forcing. Fluids **(submitted)**

Yadav S, Banerjee A, Dey T, Balasubramanian S (2016) Velocity measurements using udv in rotating annulus subjected to quasi 2d temperature variations. Int J Curr Eng Technol. doi:10.14741/Ijcet/22774106/spl.5.6.2016.40

Young R, Read P (2013) Data assimilation in the laboratory using a rotating annulus experiment. Q J R Meteorol Soc 139(675):1488–1504. doi:10.1002/qj.2061

Zurita-Gotor P, Lindzen RS (2007) Theories of baroclinic adjustment and eddy equilibration. In: Schneider T, Sobel AH (eds) The global circulation of the atmosphere, chap 2. Princeton University Press, pp 22–24. ISBN:9780691121819

Zurita-Gotor P, Vallis GK (2009) Equilibration of baroclinic turbulence in primitive equations and quasigeostrophic models. J Atmos Sci 66(4):837–863. doi:10.1175/2008JAS2848.1

Zurita-Gotor P, Vallis GK (2010) Circulation sensitivity to heating in a simple model of baroclinic turbulence. J Atmos Sci 67(5):1543–1558. doi:10.1175/2009JAS3314.1